An efficient methodology for the simulation of nonlinear irregular waves in computational fluid dynamics solvers based on the high order spectral method with an application with OpenFOAM

Young Myung Choi, Benjamin Bouscasse, Guillaume Ducrozet, Sopheak Seng, Pierre Ferrant, Eun Soo Kim, Young Jun Kim

International Journal of Naval Architecture and Ocean Engineering 15 (2023) 100510

Contents lists available at ScienceDirect

International Journal of Naval Architecture and Ocean Engineering

journal homepage: http://www.journals.elsevier.com/international-journal-of-naval-architecture-and-ocean-engineering/

An efficient methodology for the simulation of nonlinear irregular waves in computational fluid dynamics solvers based on the high order spectral method with an application with OpenFOAM

Young Myung Choi [a, b, c], Benjamin Bouscasse [a], Guillaume Ducrozet [a], Sopheak Seng [d], Pierre Ferrant [a], Eun Soo Kim [b, c], Young Jun Kim [a, b, c, *]

[a] LHEEA Lab. (ECN and CNRS), École Centrale de Nantes, Nantes, France
[b] Department of Naval Architecture and Ocean Engineering, Pusan National University, Busan, Republic of Korea
[c] Global Core Research Center for Ships and Offshore Structures (GCRC-SOP), Pusan National University, Busan, Republic of Korea
[d] Bureau Veritas - Marine & Offshore, Paris, France

ARTICLE INFO

Article history:
Received 14 June 2022
Received in revised form
12 December 2022
Accepted 12 December 2022
Available online 24 December 2022

Keywords:
HOS
CFD
Grid2Grid
Nonlinear irregular wave
Wave breaking

ABSTRACT

An efficient methodology for simulating nonlinear irregular waves in a Computational Fluid Dynamics (CFD) solver is proposed. The High Order Spectral (HOS) method is used to generate nonlinear irregular waves in an open ocean and a numerical wave tank. The inverse Fast Fourier Transforms (FFTs) and multi-dimensional interpolation from the HOS simulation results are used for the efficient reconstruction of nonlinear waves in the CFD solver. The proposed procedure is published as an open-source project called `Grid2Grid`, which is developed to interface with a generic CFD solver. It provides the function Application Programming Interface (API), which can communicate with different programming languages. Extreme wave events were used to validate the proposed procedure. The predicted wave breaking events are reported both in OpenFOAM CFD and HOS simulations, and the wave elevations of CFD during simulations show good agreement with experiments and with HOS simulation.

1. Introduction

In the ocean, structures such as ships, offshore platforms, bridges, and other marine constructions are hit by water waves, and this is of concern in naval and coastal engineering. As computational resources become increasingly powerful and many cloud services provide easy access to super-computing machines to users at competitive prices, it encourages hydrodynamicists to study nonlinear waves by solving the Navier-Stokes equations (Rhee and Stern, 2002; Shen and Wan, 2016; Bihs et al., 2017). Solving the Navier-Stokes equations in a discretized computational domain is often referred to as Computational Fluid Dynamics (CFD). CFD covers a wide range of methods, but the method commonly used to solve the Navier-Stokes equations is the Finite Volume Method (FVM) because it satisfies the conservation law in principle. The computational domain is discretized into a large number of small Finite Volumes (FVs). The associated equations are constructed in discretized form based on the principle of FV discretization (Ferziger and Peric, 2012; Jasak, 1996). The popular CFD software packages for marine applications are built based on FVM, which we refer to as CFD in the present study.

Ocean waves have many frequency components and the wave components interact with each other. As wave nonlinearity evolves with propagation, ocean waves are characterized by their randomness and nonlinearity. Due to these characteristics, generating nonlinear waves and analyzing wave-induced phenomena in CFD have been considered one of the main research topics in hydrodynamics, for instance, solitary wave propagating over the submerged breakwater (Sun et al., 2020), added resistance analysis (Lee et al., 2019), and wave energy converter simulation (Elhanafi et al., 2017).

There are several ways to generate waves in a CFD computation, the most straightforward one being the direct modelling of the wavemaker as the moving wall in the CFD. Recently, Canard et al. (2020) showed that the probability of the exceedance of the wave

* Corresponding author. LHEEA Lab. (ECN and CNRS), École Centrale de Nantes, Nantes, France.
E-mail address: youngjun.kim@pusan.ac.kr (Y.J. Kim).
Peer review under responsibility of The Society of Naval Architects of Korea.

https://doi.org/10.1016/j.ijnaoe.2022.100510

crest is strongly affected by the distance from the wavemaker in experiments. Furthermore, a large computational domain is needed to develop the waves between the wavemaker and the structure, making this methodology impractical for industrial purposes.

One way to have a smaller domain is to impose the waves at the boundary and initial conditions. The simplest representation used in the classical engineering design process is the linear superposition of Airy waves. With this technique using linear waves, the nonlinear effects associated with waves are not taken into account in the inlet/outlet and at the initial stage of simulation. Nonlinearities appear progressively during the propagation along with the CFD computational domain. This approach has similar drawbacks to using a physical wavemaker and is unsuitable for reproducing a deterministic time trace.

Another drawback of using linear waves as boundary conditions is that the nonlinear CFD solution will be different at the boundaries from the one imposed. Consequently, some reflected waves will be generated. Miquel et al. (2018) tested different wave boundaries in inlet and outlet and showed that wave reflection becomes significant in the CFD domain when a linear wave model is used. Therefore, employing nonlinear irregular waves as a target solution in CFD simulations has great advantages and some research groups used this technique to simulate nonlinear waves in the CFD solver (Kim et al., 2012; Gatin et al., 2017). Imposing fully developed nonlinear waves as the initial and boundary conditions gives an improved wave generation/absorption at the boundaries, better deterministic performances, and an enriched description of extreme events.

There has been a lot of research on the generation of long-crested irregular waves using CFD solvers (Choi and Yoon, 2009; Kim et al., 2012). However, while simulating short-crested waves in CFD is important (Chen, 2013; de Hauteclocque et al., 2017), no efficient way to generate nonlinear short-crested waves in CFD has been reported.

A nonlinear wave model based on the High-Order Spectral (HOS) method was proposed by Dommermuth and Yue (1987) and West et al. (1987), and associated research has shown that HOS models can simulate nonlinear long and short-crested irregular waves. The open-source projects HOS-Ocean and HOS-NWT were released and have been developed to simulate nonlinear waves in the ocean and the experimental wave tank used for model tests in ocean engineering (Ducrozet et al., 2007; 2012b). HOS models use Fast Fourier Transforms (FFTs) in the numerical algorithm, which results in efficient numerical results compared to other solvers (Ducrozet et al., 2012a). An additional advantage is that 3 h of simulation of irregular waves can be computed with a reasonable computational effort. Thanks to this high efficiency, Canard et al. (2022) developed a dedicated iterative procedure based on 3-h irregular wave simulations in order to control the accuracy of the wave spectrum in a numerical wave tank with HOS-NWT.

Some efforts have been made towards having a unified input wave protocol to improve the interconnection between wave solvers and CFD solvers (Bouscasse et al., 2020). This protocol has been demonstrated with wave qualification criteria in Bouscasse et al. (2021).

The present study proposes an efficient method for reconstructing 3D nonlinear wave fields from the surface potential computed by the HOS method to the CFD computational domain using the unified input wave protocol (Bouscasse et al., 2020). Because the nonlinear waves are already simulated with the HOS method, we can simulate the extreme wave event in the CFD simulation for a short duration. This procedure can reduce the computational cost, encouraging the practical applications of CFD simulation in wave-structure interaction problems. The volumetric information of the HOS fields in CFD simulation requires the evaluation of field quantity at any arbitrary point. However, the computational grid of the HOS method is relatively coarser than those of the CFD simulation. Therefore, the three- or four-dimensional B-spline interpolations in space and time are used to reconstruct wave quantities at an arbitrary position and time for efficiency. The proposed procedure is applied to the HOS-Ocean and HOS-NWT wave models, and those are applied for long- and short-crested irregular wave generation in CFD simulation. Gatin et al. (2017) applied the HOS-Ocean wave model in the CFD-simulation, Lu et al. (2022) introduces the GPU-accelerated HOS simulation for the simultaneous HOS and CFD simulation to simulate wave-current interaction for the naval application. However, the wave generation using the HOS-NWT model has not been studied yet to the author's best knowledge. The measured waves in the model basin can be reproducible with the HOS-NWT model; therefore, these waves can be simulated in the CFD simulation with the proposed methodology.

The present paper is divided as follows. First, the background theory on the HOS wave models is shortly reviewed. Second, the HOS wave field reconstruction algorithm and the three- and four-dimensional B-spline interpolation methodology are presented. Then, a CFD solver based on the OpenFOAM used for the validation is presented. Finally, the nonlinear HOS long- and short-crested irregular waves from different HOS wave models are generated in the CFD simulations for different wave conditions. Furthermore, the wave breaking event predicted by the HOS-NWT simulation is also reported both in experiment and CFD simulation.

2. Wave models

2.1. Linear theory and associated research on irregular waves

The simplest method to generate irregular waves is the superposition of linear regular waves with random phases as:

$$\Phi(x,y,z,t) = \sum_{j=1}^{N_{head}} \sum_{i=1}^{N_{freq}} \frac{igA_{ij}}{\omega_i} \frac{\cosh k_i(z+h)}{\cosh k_i h} e^{-i(k_i(x\cos\beta_j + y\sin\beta_j) - \omega_i t + \delta_{ij})}, \tag{1}$$

where $\omega_i^2 = gk_i\tanh(k_i h)$ is wave frequency, h is water depth, k_i is wavenumber, and β_j is the directional angle of wave. N_{head} and N_{freq} are numbers of heading and frequency of waves, respectively. δ_{ij} is the random phase. A_{ij} is the wave amplitude which is given in

$$A_{ij} = \sqrt{2S(\omega_i)D(\omega_i|\beta_j)\Delta\theta_i\Delta\omega_i} \tag{2}$$

where $S(\omega)$ is the wave spectrum and $D(\omega|\beta)$ is a directional spreading function, satisfying $\int_{\beta_{\min}}^{\beta_{\max}} D(\omega|\beta)d\beta = 1$, respectively. Many types of wave spectrum and directional spreading functions have been proposed. A comprehensive summary can be found in the study of Goda (1999).

The linear superposition is associated with the fact that frequency components do not interact with each other, which is not true in reality. Forristall (2000) showed the importance of second-order effects on the crest distribution with real measurements. Furthermore, associated research has explained the generation mechanism of rogue waves with wave nonlinearity (Baronio et al., 2015; Fedele et al., 2016).

2.2. Nonlinear irregular waves: open-ocean

The High-Order Spectral (HOS) method, based on a pseudo-spectral approach, is used to simulate nonlinear wave

propagation efficiently (Dommermuth and Yue, 1987; West et al., 1987). In the open-ocean configuration, a rectangular computational domain is considered with its horizontal lengths L_x and L_y along the x and y directions, respectively, with the flat sea bottom located at $z = -h$. Periodic lateral boundary conditions are considered. With this configuration, the power density spectra and the wave crest statistics are homogeneous in space but vary in time.

Assumptions of an ideal fluid and irrotational flow are employed, and the free-surface $\Xi(x, y, t)$ is assumed to be continuous and a single-valued function. Therefore the free-surface can be represented by $F(x, y, z, t) = z - \Xi(x, y, t) = 0$. The free-surface potential $\varphi(x, y, t) = \Phi(x, y, z = \Xi, t)$ is introduced, where $\Phi(x, y, z, t)$ is the velocity potential in the fluid domain. The kinematic and dynamic free-surface boundary conditions on the free-surface potential are given as follows:

$$\frac{\partial \varphi}{\partial t} = -g\Xi - \frac{1}{2}\nabla\varphi \cdot \nabla\varphi + \frac{1}{2}w^2(1 + \nabla\Xi \cdot \nabla\Xi) \tag{3}$$

$$\frac{\partial \Xi}{\partial t} = -\nabla\varphi \cdot \nabla\Xi + w(1 + \nabla\Xi \cdot \nabla\Xi) \tag{4}$$

where w is the vertical velocity at the free-surface. $\nabla = (\partial_x, \partial_y)$ is the horizontal differential operator. For the open-ocean wave propagation problem simulation, the velocity potential (Φ) and the vertical velocity are expanded in perturbation series with a small parameter $\varepsilon = kA$ representing the wave steepness.

$$\Phi(x, y, z, t) = \sum_{m=1}^{M} \Phi^{(m)}(x, y, z, t) \tag{5a}$$

$$w(x, y, t) = \sum_{m=1}^{M} w^{(m)}(x, y, t) \tag{5b}$$

Here, $q^{(m)}$ denotes a quantity of $O(\varepsilon^m)$, and M is the nonlinear order of the HOS method. In a rectangular computational domain, the free-surface potential and wave elevation can be expressed with a series of modal functions (Dommermuth and Yue, 1987; West et al., 1987):

$$\varphi(x, y, t) = \sum_{i=1}^{N_x} \sum_{j=1}^{N_y} B_{ij}^{\varphi}(t) \exp(\mathrm{i}k_{x,i}x) \exp(\mathrm{i}k_{y,j}y) \tag{6a}$$

$$\Xi(x, y, t) = \sum_{i=1}^{N_x} \sum_{j=1}^{N_y} B_{ij}^{\Xi}(t) \exp(\mathrm{i}k_{x,i}x) \exp(\mathrm{i}k_{y,j}y) \tag{6b}$$

where $B_{ij}^{\varphi}(t)$ and $B_{ij}^{\Xi}(t)$ are modal amplitudes of the free-surface potential and the free-surface elevation, respectively. The horizontal directional wavenumbers $k_{x,i} = \frac{2\pi i}{L_x}$ and $k_{y,j} = \frac{2\pi j}{L_y}$ are set using the horizontal domain dimensions. Modal amplitudes such as $B_{ij}^{\varphi}(t)$ and $B_{ij}^{\Xi}(t)$ are calculated from the wave spectra and set at the initial time step. As the simulation goes on, the modal amplitudes evolve due to nonlinearity. Details about HOS-Ocean are given in Ducrozet et al. (2007), Bonnefoy et al. (2009), and Ducrozet et al. (2016).

2.3. Nonlinear waves: Numerical Wave Tank(NWT)

Simulating wave propagation with an open ocean configuration does not guarantee the stability of wave spectra and wave statistics in time, and this is an issue for some engineering problems. For this reason, it is useful to define a domain with a wavemaker and a numerical beach on the opposite side, which is the simplest representation of a numerical wave tank. Nonlinear waves in the three-dimensional numerical rectangular tank can also be simulated by the HOS model. In this case, the kinematic lateral boundary conditions are given as:

at the wavemaker

$$\frac{\partial X_{wm}}{\partial t} = \frac{\partial \Phi}{\partial x} - \frac{\partial X_{wm}}{\partial y}\frac{\partial \Phi}{\partial y} - \frac{\partial X_{wm}}{\partial z}\frac{\partial \Phi}{\partial z} \tag{7a}$$

at other walls and the tank bottom:

$$\frac{\partial \Phi}{\partial n} = 0 \tag{7b}$$

where $x = X_{wm}(y, z, t)$ is the x-directional displacement of the wavemaker. The total flow q is decomposed into a harmonic flow q_H and a local flow q_L to account for these kinematic conditions at the lateral boundaries.

$$q(x, y, z, t) = q_H(x, y, z, t) + q_L(x, y, z, t) \tag{8}$$

Here q represents the flow quantity, such as the velocity potential and the fluid velocity. Then, the velocity potential is decomposed into the harmonic and local velocity potentials as $\Phi = \Phi_H + \Phi_L$. The harmonic potential satisfies the wall condition $\frac{\partial \Phi_H}{\partial n} = 0$ on the wavemaker, and the local potential satisfies the wavemaker condition:

$$\frac{\partial \Phi_L}{\partial x} - \frac{\partial X_{wm}}{\partial t} = Q_{wm}(y, z, t) \tag{9}$$

where $Q_{wm}(y, z, t)$ is the nonlinear forcing term depending on the order of approximation. In the HOS-NWT model, the nonlinear forcing term up to the third-order is considered. The details of wavemaker modelling are well described in Ducrozet et al. (2012b). Similar to what was done with the HOS-Ocean model, the pseudo-spectral method is applied both for the harmonic and local flows, and FFTs are used to obtain the two flow quantities to ensure computation efficiency. An absorbing beach with numerical damping is modelled at the end of the computational domain to dampen the propagating waves in the numerical wave tank. Furthermore, Seiffert et al. (2017) and Seiffert and Ducrozet (2018) take into account the dissipation effect due to wave breaking by introducing a wave breaking model. HOS results were validated against experimental results.

3. Generation of propagating waves in the CFD solver

Many choices exist for wave generation in the CFD solver: (1) generation of waves by considering the wavemaker at a boundary; (2) forcing the known analytic and numerical wave solutions in the CFD solver as initial and boundary conditions, e.g. One-way coupling and (3) solving both waves and viscous flow and delivering each solution to update each model, e.g. Two-way coupling. The first and the third procedures induce a huge computational cost making these solutions inefficient for practical purposes. Many researchers use the second procedure to solve wave-structure interaction problems (Jacobsen, 2017; Kim et al., 2012; Engsig-Karup and Eskilsson, 2019). Recently, Bouscasse et al. (2020) suggested a unified one-way coupling protocol for the generation of waves in CFD solvers.

In the present study, we adopted the one-way coupling procedure for wave generation. After simulating the waves with the HOS method, the modal amplitudes of free-surface velocity potentials and wave elevation are saved. Because the modal

amplitudes and functions are known, the flow quantities can be reconstructed spatially at any arbitrary point of the computational domain. The interpolation with respect to time interval is necessary because time stepping is rarely synchronized. However, the computational costs increase rapidly when the reconstruction is applied for short-crested waves because it needs the superposition of the x and y-directional (and z-directional for HOS-NWT) modes at millions/billions of computational points in the CFD domain at each CFD time step. It is not practical for simulating short-crested waves. Therefore, the reconstruction based on the inverse Fast Fourier transforms(FFTs) (Frigo and Johnson, 2005) over a regular grid (Surf2Vol) where multi-dimensional interpolation (Vol2Vol) is adopted for efficiency. The schematic view of the computational procedure is shown in Fig. 1.

The proposed reconstruction procedure is programmed and published as the open-source project `Grid2Grid` with a GPLv3 license (Choi et al., 2019). The structure of `Grid2Grid` is depicted in Fig. 2. The surfacic HOS results containing modal amplitudes are used to construct the volumetric HOS wavefields at each HOS time step (Surf2Vol). The Fast Fourier Transform is used for efficient reconstruction in this step. Then, multiple HOS wave fields computed over successive HOS simulation time steps are used in the subsequent interpolation in the points and time step of the final grid (Vol2Vol). Then, the API (Application Programming Interface) function, which follows the ISO_C_BINDING rule, transfers the time and space variables and physical quantities. This way, `Grid2Grid` can be connected to any CFD solver whose API functions follow the ISO_C_BINDING rule.

Some important API functions of `Grid2Grid` are summarized in Table 1. By using these API functions, the `Grid2Grid` library can be initialized and updated to simulate nonlinear waves in the CFD solver. Some examples written in Fortran and OpenFOAM (C++) are given in the `Grid2Grid` package to provide a straightforward implementation example for CFD developers.

3.1. Reconstruction of a HOS wavefield over a regular grid (Surf2Vol)

As described in Fig. 1, the HOS wave fields are reconstructed on a regular interpolation grid to take advantage of the efficiency of FFTs. Then, interpolation is used for efficient reconstruction on the computational grid of CFD. Therefore, the regular interpolation grid needs to be refined sufficiently to minimize the interpolation error. The interpolation error with respect to the resolution of the interpolation grid is investigated. Basis functions for horizontal and vertical directions are sinusoidal and hyperbolic functions, therefore the two functions given in Eq. (10) are adopted to evaluate the interpolation error.

$$f(x) = \cos kx \qquad \text{for} \qquad 0 \le x \le \lambda \tag{10a}$$

$$g(z) = \quad e^{kz} \qquad \text{for} \qquad -\infty \le z \le 2H \tag{10b}$$

It should be noted that the above two functions correspond to basis functions for deep water conditions. The wavenumber is taken to be $k = 2\pi$ to have a unit wavelength, and the wave height is $H = 0.14\lambda$ which is regarded as the breaking limit of ocean waves. The exact values of the two functions are given on the regular grid with different discretizations, and the interpolation error with respect to the horizontal and vertical refinement of the interpolation grid is tested. In the horizontal direction, the number of refinements corresponds to the number of cells per wavelength. The number of refinements in the vertical direction is the number of cells per wave height. The maximum errors are defined in Eq. (11), where q_I is interpolated quantity.

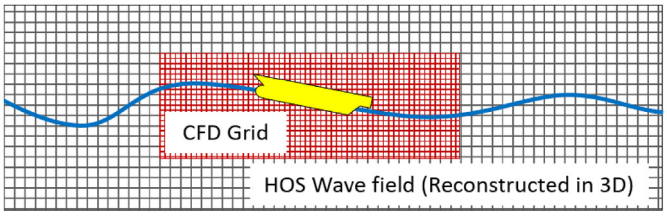

Fig. 1. Interpolation from HOS wave field to CFD computational grid.

$$\varepsilon^x = \frac{\max |f_I(x) - f(x)|}{\int_0^\lambda f(x)dx} \qquad x \in [0, \lambda] \tag{11a}$$

$$\varepsilon^z = \frac{\max |g_I(z) - g(z)}{\int_{-\infty}^0 g(z)dz} \qquad z \in (-\infty, 0] \tag{11b}$$

Fig. 3 presents the interpolation errors of the two test functions. As the number of refinements increases, the interpolation errors decrease. Furthermore, the order of accuracy with respect to interpolation orders follows well the expected order of accuracy, which is represented as a dashed line in Fig. 3.

To achieve an interpolation error of less than 10^{-6} with CUBIC interpolation, the number of regular grids for horizontal and vertical directions should be at least 60 per wavelength and 30 per wave height for regular waves, respectively. Recently, Canard et al. (2020) suggested a qualification criterion for irregular waves to qualify the wave spectrum in the range of $f = [\frac{3}{4}f_p, \frac{3}{2}f_p]$ with f_p as the peak frequency of the corresponding spectrum. Therefore, the suggested interpolation refinement criterion in the regular grid can be used with the reference wavelength, which corresponds to $f_{cri} = \frac{3}{2}f_p$.

3.2. Interpolation from HOS wave field (Vol2Vol)

After reconstructing the nonlinear waves over the computational grid, a B-spline interpolation is used to reconstruct the nonlinear wavefields at a set of arbitrary positions and times because of the time steps of the HOS solver and the CFD solver, which are, in principle, different. A functional value $f(\mathbf{s})$ can be determined by multi-dimensional variables, $\mathbf{s} = (s_1, s_2, \ldots, s_N)^T$, where s_i represents a set of independent coordinates and N is the number of dimensions. Known functional values at interpolation nodes $s_{i_1}, s_{i_2}, \ldots, s_{i_N}$ are defined. For example, $\mathbf{s} = (s_1, s_2, \ldots, s_N)^T$ are the arbitrary position and time of the CFD solver, and the HOS wave fields are reconstructed at interpolation nodes $s_{i_1}, s_{i_2}, \ldots, s_{i_N}$. Then, the interpolated function value can be evaluated as:

$$\begin{aligned} &f(s_1, s_2, \ldots, s_N) \\ &= \sum_{i_1, i_2, \ldots, i_N = -m}^{m+1} f(s_{i_1}, s_{i_2}, \ldots, s_{i_N}) \prod_{j=1}^{N} B_i^{(p)}(s_j) \\ &m = \mathrm{int}(N_{\mathrm{interp}}/2), \quad p = N_{\mathrm{interp}} - 1 \end{aligned} \tag{12}$$

where N_{interp} is the interpolation order, e.g. $N_{\mathrm{interp}} = 1, 2, 3$ represent the linear, quadratic and cubic interpolations, respectively. The B-spline function $B_i^{(p)}(s_j)$ can be expressed with the recursion relation:

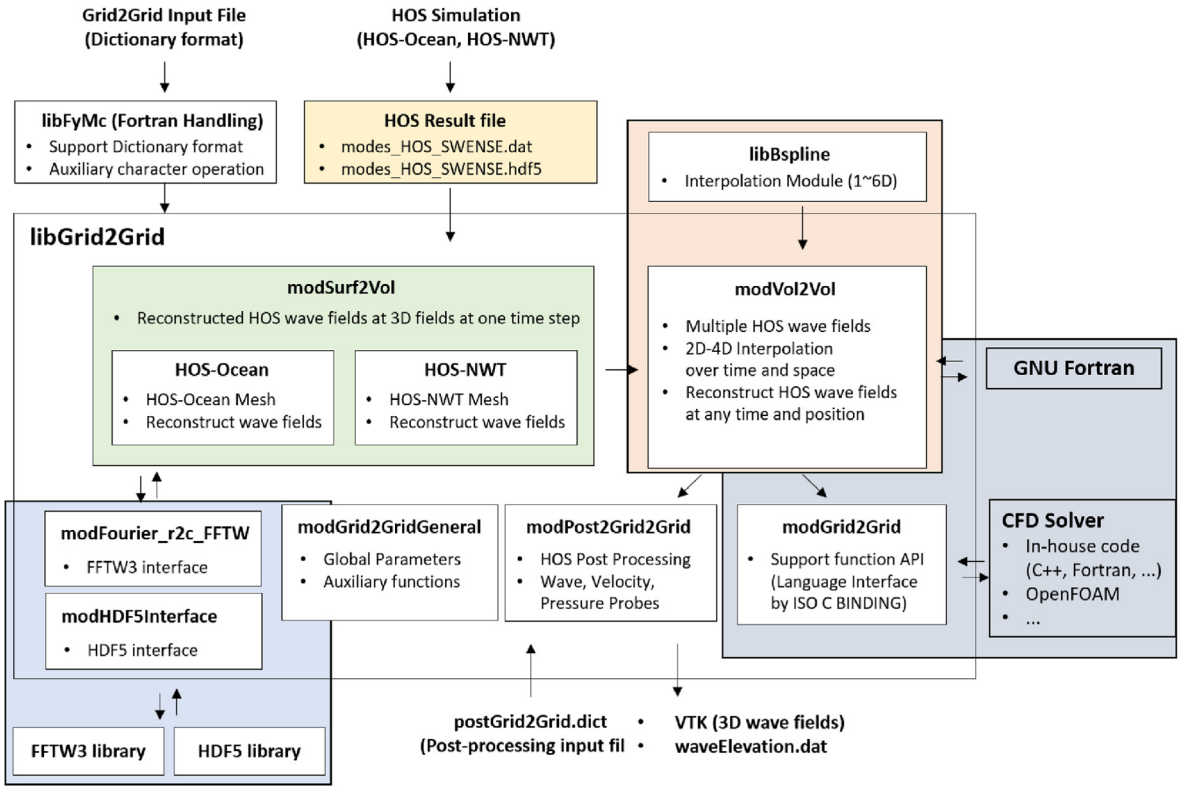

Fig. 2. The structure of Grid2Grid and the reconstruction algorithm and its interface.

Table 1
Some important API functions of `Grid2Grid`, the prefix of the API function's name: __modgrid2grid_MOD_.

Function name	Functionality
initializegrid2grid	Initialize `Grid2Grid` with input
correctgrid2grid	Update HOS wave fields
gethoseta	Get wave elevation
Gethosu	Get fluid velocity
gethospd	Get dynamic pressure
gethosendtime	Get HOS simulation end time
gethoswaterdepth	Get HOS water depth
isgrid2gridinitialized	Check `Grid2Grid` is initialized

$$B_i^{(0)}(s_j) = \begin{cases} 1 & \text{if} \quad s_{j_i} \le s < s_{j_{i+1}} \\ 0 & \text{otherwise} \end{cases} \tag{13a}$$

and

$$\begin{aligned} B_i^{(n)}(s_j) &= \frac{s - s_{j_i}}{s_{j_{i+p}} - s_{j_i}} B_i^{(n-1)}(s_j) \\ &+ \frac{s_{j_{i+p+1}} - s}{s_{j_{i+p+1}} - s_{j_{i+1}}} B_{i+1}^{(n-1)}(s_j) \quad n \ge 1 \end{aligned} \tag{13b}$$

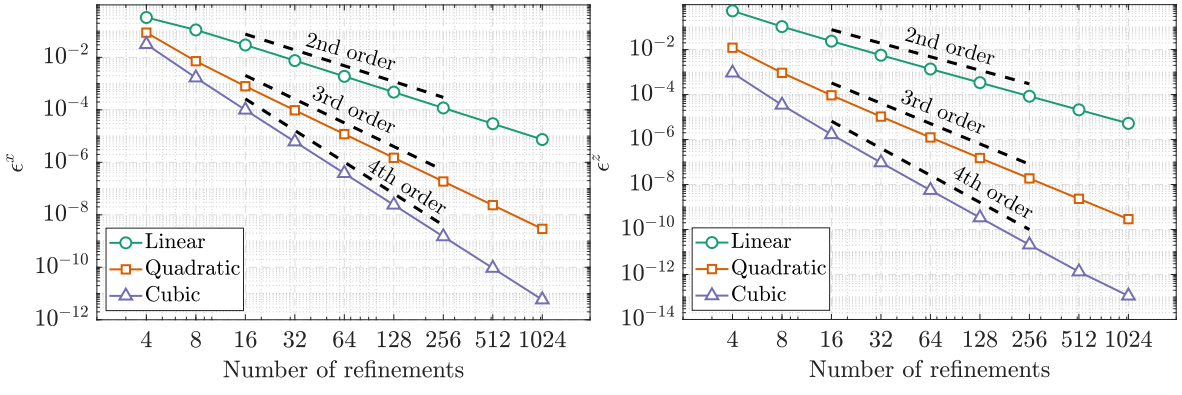

(a) Cosine function (b) Exponential function

Fig. 3. Interpolation errors with respect to refinement for two test functions.

Instead of computing the spline functions at each time, De Boor (1978) proposed an equivalent recursion formula for better efficiency. Posing $C^{(0)}_{i_1,i_2,\cdots i_N} = f(s_{i_1}, s_{i_2}, \ldots, s_{i_N})$ and substituting the B-spline recursion formula into Eq. (12), we obtain

$$f(s_1, s_2, \ldots, s_N) = \sum_{i_1,i_2,\ldots,i_N=-m}^{m+1} C^{(p)}_{i_1,i_2,\cdots i_N} \tag{14a}$$

with the recursion relation of $C^{(n)}_{i_1,i_2,\cdots i_N}$:

$$\begin{aligned} C^{(n)}_{i_1,i_2,\cdots i_N} &= \left(1 - w^{(n)}_{j,i,p}\right) C^{(n-1)}_{i_1-1,i_2-1,\cdots i_N-1} \\ &\quad + w^{(n)}_{j,i,p} C^{(n-1)}_{i_1-1,i_2-1,\cdots i_N-1} \end{aligned} \tag{14b}$$

with

$$w^{(n)}_{j,i,p} = \frac{s - s_{j_i}}{s_{j_{i+p+1-n}} - s_{j_i}} \tag{14c}$$

This alternative way is called *de Boor's algorithm*. Fig. 4 shows the distribution of the B-spline functions used for the cubic interpolation.

It implies that only a few successive HOS wave fields at $t = t_1^{HOS}$, $t_2^{HOS}, \cdots t_{N_t^{HOS}}^{HOS}$ near the CFD simulation time t_{CFD} are necessary for the interpolation. There always exist two successive instants where $t_j^{HOS} \leq t_{CFD} < t_{j+1}^{HOS}$, and successive HOS wave fields are presented in Fig. 5.

By adopting this interpolation procedure, we do not need to reconstruct the HOS wave fields for the whole HOS simulation time. It is sufficient to know successive HOS wave fields with moving interpolation time windows. Therefore, computational memory in the HOS reconstruction step can be saved.

3.3. Interpolation enhancement by zero-padding

The modal functions used in the HOS model are trigonometric or hyperbolic functions. However, the B-spline functions used for the interpolation are piece-wise polynomials near interpolation nodes. For wave propagation, HOS models require limited spatial discretization to reach a high level of accuracy. Typically, only O(10) points per wavelength are used thanks to the pseudo-spectral formalism of HOS solvers and the corresponding convergence rate (Ducrozet et al., 2012b,a). A large spacing (Δx, Δy) in the HOS domain will give a large interpolation error. To minimize the interpolation error due to large spacing, a zero-padding scheme is introduced to reconstruct the HOS waves on a refined grid. Additional zero amplitudes corresponding to high wavenumbers are introduced intentionally. After applying the inverse FFTs, the HOS wave field is reconstructed on a more refined HOS grid compared to the original HOS grid. The schematic view of the zero-padding scheme is shown in Fig. 6.

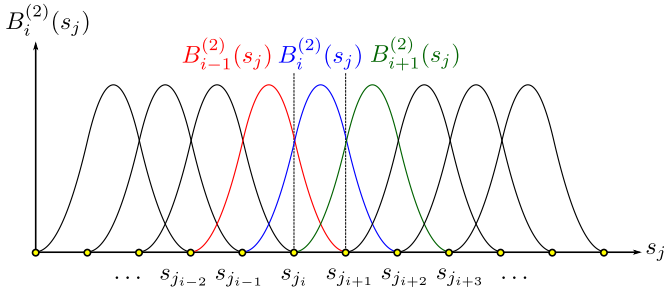

Fig. 4. Distribution of B-spline curves used for the cubic interpolation.

Li (2018) tested the B-spline interpolation order and zero-padding scheme by reconstructing the HOS wave fields on a CFD grid. The study showed that using a low interpolation order with a marginally large spacing of the HOS domain may result in large continuity errors in the CFD computation. However, it can be improved by using a high interpolation order with the zero-padding technique. In the present study, the interpolation order of $p = 3$ (Cubic-interpolation) is used in temporal and spatial interpolation, and the numerical grid of HOS is refined enough to minimize the interpolation error. The interpolation refinement corresponds to the case of $\lambda\Delta x > 50$ and $H/\Delta z > 16$. The interpolation error in Fig. 3 shows less than $10^{-}5$ with this configuration.

4. CFD solver

`foamStar` is an in-house code co-developed by Bureau Veritas and École Centrale de Nantes within the framework of OpenFOAM to solve wave-structure interaction problems. It is based on the multi-phase flow solver `interDymFoam` (Rusche, 2002; Damián, 2013) in the OpenFOAM package (Weller et al., 1998; Jasak, 2009). The wave generation module is based on the open-source project `waves2Foam` (Jacobsen et al., 2012; Jacobsen, 2017). The mechanical solver is developed to simulate the dynamics of rigid or elastic marine structures (Seng et al., 2014).

The free-surface is captured by the Volume of Fluid (VOF) method (Hirt and Nichols, 1981). The governing equations describing multi-phase flow are given as follows:

$$\nabla \cdot \mathbf{u} = 0 \tag{15a}$$

$$\begin{aligned} \frac{\partial(\rho\mathbf{u})}{\partial t} + \nabla\cdot(\rho\mathbf{u}\mathbf{u}^T) - \nabla\cdot\left[\mu\left(\nabla\mathbf{u} + \nabla\mathbf{u}^T\right)\right] = \\ -\nabla p_d - (\mathbf{g}\cdot\mathbf{x})\nabla\rho \end{aligned} \tag{15b}$$

$$\frac{\partial\alpha}{\partial t} + \nabla\cdot(\alpha\mathbf{u}) + c_\alpha\nabla\cdot\left[\mathbf{u}_n^f\alpha(1-\alpha)\right] = 0 \tag{15c}$$

where ρ, $\mathbf{u}$, p_d and $\mathbf{g} = (0, 0, -g)$ are the density, the velocity, and the dynamic pressure of the air-water mixture and the gravitational acceleration vector, respectively. α is the VOF representing the ratio of occupied water volume to computational cell volume. The third term in Eq. (15c) gives an artificial surface compression in the normal direction to keep a sharp air-water interface (Rusche, 2002). c_α and $\mathbf{u}_n^f$ are the α-compression coefficient and free-surface normal velocity, respectively. This term only works if $\alpha \in (0, 1)$. The mixture density and viscosity are given as follows:

$$\rho = \rho_w\alpha + \rho_a(1-\alpha) \tag{16a}$$

$$\mu = \mu_w\alpha + \mu_a(1-\alpha) \tag{16b}$$

where q_w and q_a represent quantities associated with water and air, respectively.

The generation/absorption of waves in `foamStar` is modelled by using an explicit relaxation scheme that blends the computed flow quantities with the target quantities (Mayer et al., 1998; Fuhrman, 2004; Engsig-Karup, 2006). The CFD domain is divided into a central "pure CFD" zone where only the viscous flow equations apply and one or several relaxation zones that are set at lateral boundaries. In these zones, the flow quantities are relaxed after solving the equations as:

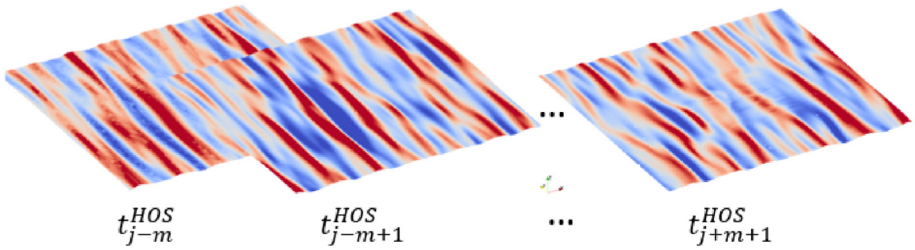

Fig. 5. Reconstructed HOS wave fields over successive HOS simulation times for the interpolation.

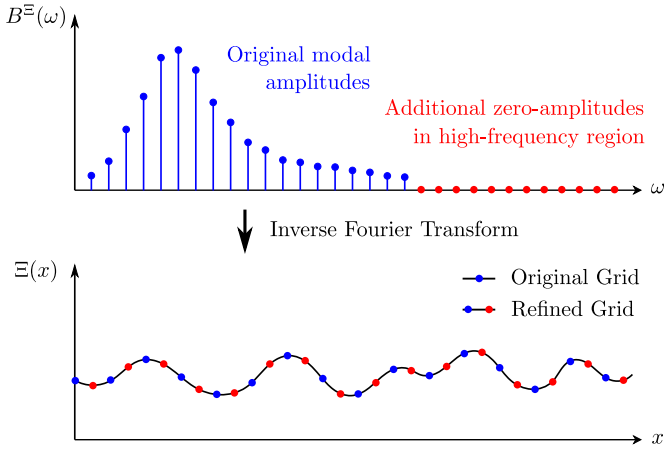

Fig. 6. Interpolation enhancement by zero-padding to increase the spatial resolution.

$$\chi = (1-w)\chi + w\chi^{\text{Target}} \tag{17}$$

where χ is the flow quantity, χ^{Target} is the target quantity, and $w \in [0, 1]$ is the weight function, respectively. w is a function that progressively varies over the relaxation zone. At the boundary with the "pure CFD" zone $w = 0$ to ensure continuity, and at the lateral boundaries of the entire domain $w = 1$ so that the solution is exactly the target solution. The schematic view of the computational domain is shown in Fig. 7.

The choice of weight function affects the magnitude of reflected waves. Many studies have shown that a properly chosen weight function with a marginal size of the relaxation zone can minimize wave reflections at the boundaries (Miquel et al., 2018; Perić et al., 2018; Choi et al., 2020).

Perić et al. (2018) investigated the effect of weight function on the wave propagation simulation. They showed that while an optimized relaxation scheme can minimize undesirable waves, undesirable waves are inevitable if the relaxation scheme is adopted for the generation and absorption of waves. Recently, Kim (2021) conducted wave propagation simulations considering

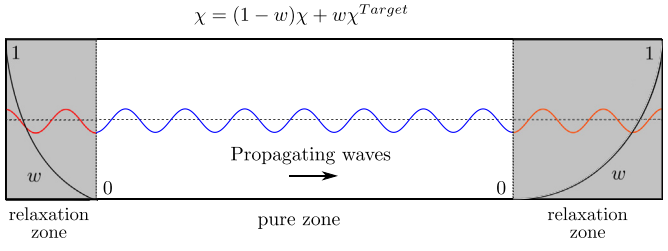

Fig. 7. Schematic view of computational domains for the wave propagation.

turbulence effects based on the stabilized turbulence model for free-surface flow proposed in Larsen and Fuhrman (2018). He showed that propagating waves preserve their amplitudes for a long simulation time.

5. Results and discussion

5.1. Generation of HOS waves in the CFD solver

To validate the procedure of nonlinear wave generation in the CFD solver, a total of six wave conditions, given in Table 2, are considered within the two HOS models. Since the wave generation mechanism is different for HOS-Ocean and HOS-NWT solvers, it is not possible to deterministically compare waves from two HOS solvers. Therefore, the present study tried to check the capability of the procedure of nonlinear wave generation in the CFD solver using random wave conditions. The JONSWAP spectrum is used to describe the frequency spectrum ($S(f)$) of irregular waves. A directional spreading function in Eq. (18) is introduced for short-crested waves, where σ is the bandwidth of the directional spreading function (Dysthe et al., 2003).

$$D(\beta) = \frac{1}{\sigma}\cos^2\left(\frac{\beta}{4\sigma}\right) \tag{18}$$

The computational domain of the CFD solver is set to be $x \in [0, 6\lambda_{ref}]$ and $z \in [-h, h]$ for 2D wave simulation, where λ_{ref} is the reference wavelength, e.g. $\lambda_{ref} = \lambda$ for regular waves, $\lambda_{ref} = \lambda_p$ for irregular waves, and λ_p is the wavelength corresponding to the peak wave period (T_p). The same x and y-directional length $(x, y) \in [0, 6\lambda_{ref}]$ and height $z \in [-h, h]$ are used in the 3D simulations. The spatial refinement is conducted uniformly in the horizontal direction. Since the waves have a hyperbolic velocity profile in the vertical direction, a variable refinement is applied in this direction. Three different zones are set: (1) Underwater zone $z \in [-h, -H_{ref}]$, (2) Free-surface zone $z \in [-H_{ref}, H_{ref}]$ and (3) Air zone $z \in [H_{ref}, h]$. The reference wave height is $H_{ref} = H$ for regular waves and $H_{ref} = H_s$ for irregular waves. The free-surface zone is refined uniformly, and a geometric progression is applied to the other zones (`simpleGrading` in OpenFOAM) to keep a dense spatial resolution in the free-surface zone and to maintain a smooth change of cell heights. The value for `simpleGrading` is taken as 5 from the results of Choi et al. (2020), e.g. the highest and the lowest cell height ratio is 5 in underwater and air zones. The spatial refinement is performed such that $\lambda_{ref}/\Delta x = 125$ and $H_{ref}/\Delta z \geq 20$ for 2D wave simulation and $\lambda_{ref}/\Delta x = \lambda_{ref}/\Delta y = 50$ and $H_{ref}/\Delta z \geq 15$ for 3D wave simulation, respectively. The number of computational cells is reduced for the 3D wave elevation in order to limit the computational cost, e.g. the number of cells in 3D simulations is $O(10^6)$. The length of the relaxation zones is taken to be twice the reference wavelength, $L_{relax} = 2\lambda_{ref}$. The pure CFD zone is the computational domain where no relaxation scheme is applied, and its size is twice the reference wavelength. The computational domain and the numerical grid

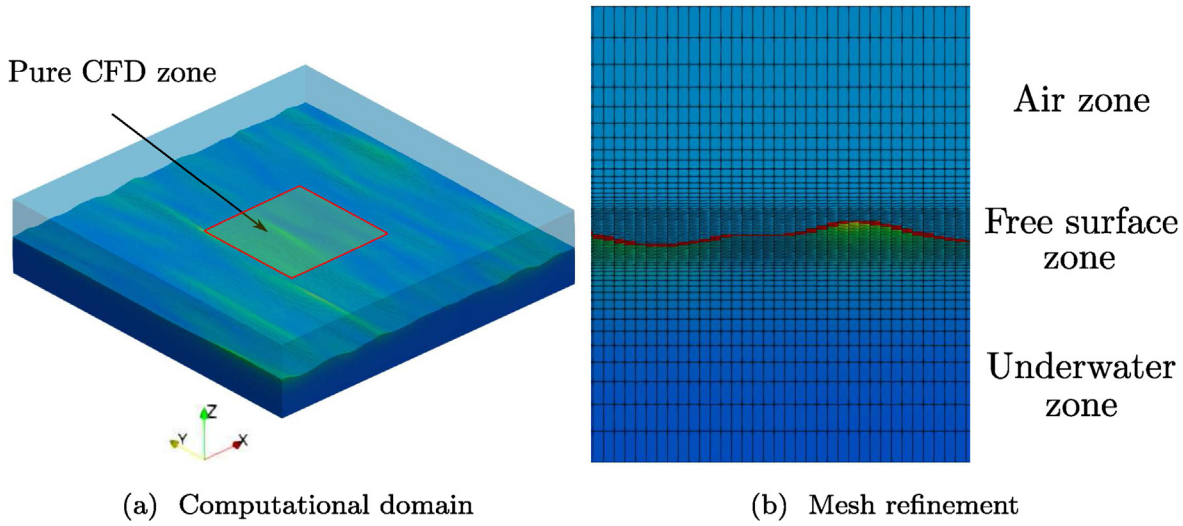

Fig. 8. The computational domain and mesh refinement for the simulation of short-crested waves (HOS-NWT 3D irregular waves).

Table 2
Wave conditions used for each HOS model to reconstruct the nonlinear waves in the CFD solver, T: wave period, H: wave height, T_p: peak period, H_s: significant wave height, γ: magnification factor in JONSWAP spectrum, σ: bandwidth of directional spreading function in Dysthe et al. (2003).

Wave Type	Item	HOS-Ocean	HOS-NWT
Regular Waves (2D)	$T[s]$	–	0.702
	$H[m]$	–	0.0431
Irregular Waves (2D)	$T_p[s]$	0.702	1.0
	$H_s[m]$	0.0288	0.05
	γ	3.3	3.3
Regular Waves (3D)	$T[s]$	–	0.702
	$H[m]$	–	0.0288
	$\beta[^\circ]$	–	60°
Irregular Waves (3D)	$T_p[s]$	1.000	0.702
	$H_s[m]$	0.100	0.0384
	γ	3.3	3.3
	σ	0.3	0.3

used for the HOS-NWT 3D irregular waves during the simulation are shown in Fig. 8.

The wave fields in the CFD domain are initialized with the reconstructed HOS wave fields, and then the waves in the CFD domain are generated and absorbed in the relaxation zones during the simulation. The simulation snapshots of 3D wave fields in CFD with different HOS wave models are shown in Fig. 9.

Three-dimensional wave fields in CFD are well simulated, and the smooth transition between the pure CFD zone and the relaxation zone is shown. The wave elevation is measured at the center of the pure CFD zone and compared with the result of the HOS simulation.

The comparison between the reference HOS simulation and the reconstructed waves in the CFD solver is shown in Fig. 10. Simulation time is normalized with reference period, $T_{ref} = T$ and $T_{ref} = T_p$ for regular and irregular waves, respectively. At the initial time, both CFD and HOS references show good agreement because the wavefields are initialized with HOS wavefields. A small increase in discrepancies of waves between CFD and HOS is shown as the simulation progresses, but the wave elevations show good agreement overall. The discrepancy between wave elevations of HOS and CFD simulations could be due to: (1) insufficient refinement of the computational mesh used in CFD, which results in numerical damping, (2) an interpolation error due to the interpolation order and the number of interpolations points, (3) undesirable waves due to the weight function in the relaxation zone, respectively. It is expected that on the spatial and temporal scales studied, the effect of viscosity (acting in the bulk of the fluid as well as at the air/water interface) is negligible. For both long-crested (graph (a), (c), (d), and (e)) and short-crested (graph (b) and (f)) cases, the proposed CFD wave generation procedure generally works well. However, a larger difference between CFD and HOS waves is found for the short-crested wave condition due to the lower mesh refinement.

The reference HOS wave elevation Ξ_{HOS} and the surface elevation of the CFD solver Ξ_{CFD} are compared by evaluating a Pearson correlation coefficient (r) between the two time-series data. The Pearson correlation coefficient of wave elevations is defined as in Hogg et al. (2005):

$$r = \frac{\mathrm{cov}(\Xi_{HOS}, \Xi_{CFD})}{\sigma_{HOS}\sigma_{CFD}} \tag{19}$$

where $\mathrm{cov}(\Xi_{HOS}, \Xi_{CFD})$, σ_{HOS} and σ_{CFD} represent the covariance and the standard deviations of wave elevations obtained from HOS and CFD simulations for the entire CFD simulation time, respectively. The Pearson correlation coefficient (r) measures a linear correlation between two data sets which always have a value between $r = -1$ and $r = 1$. When $0 < r \leq 1$, two sets of data have a positive correlation, and when $0 < r \leq 1$, they have a negative correlation. When $r = 0$, two data sets have no relationship. The computed Pearson correlation coefficient(r) for different simulations is given in Table 3 over the whole CFD simulation time. The waves simulated by the CFD solver show a good correlation with reference HOS simulations.

5.2. Coupling in breaking sea states and comparison with experiments

The nonlinear wave generation procedure in the CFD solver was validated with experimental results. The experiments were conducted in the 3D wave tank at the École Centrale de Nantes. The dimensions of the wave tank are shown in Fig. 11. Its length, width, and water depth are 46.4 m, 29.7 m, and 5 m. Forty-eight segmented wavemakers are installed at one side to generate various types of waves, including directional waves. The width of the segmented wavemaker is 0.6 m. A wave beach of 9.7 m long is installed at the opposite side of the wavemakers to absorb waves.

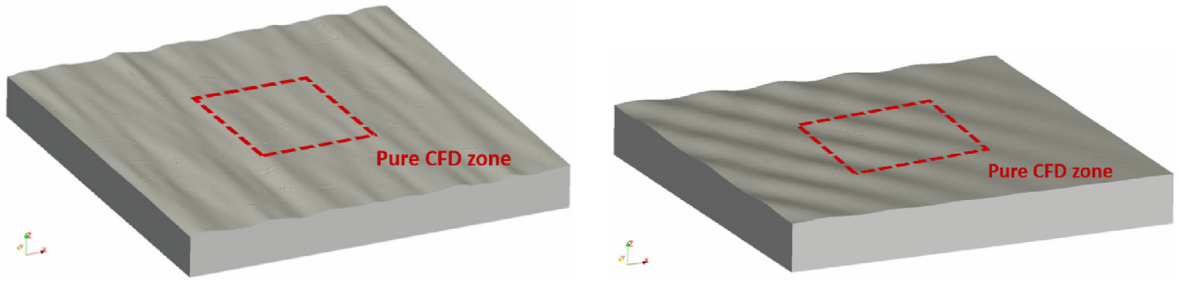

(a) HOS-Ocean (3D irregular waves) (b) HOS-NWT (3D oblique regular waves)

Fig. 9. Simulated HOS wave fields in CFD.

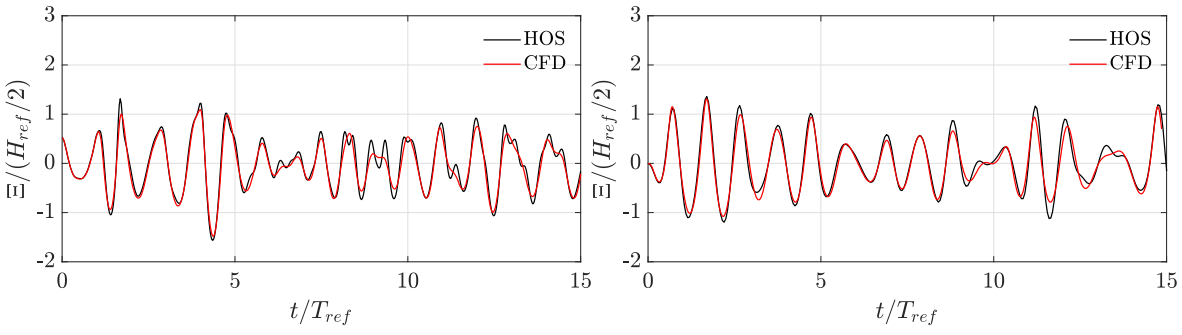

(a) HOS-Ocean 2D Irregular waves (b) HOS-Ocean 3D Irregular waves

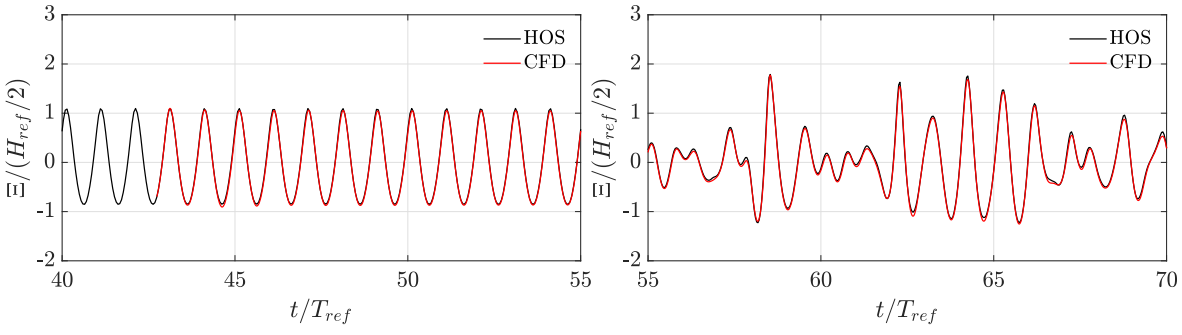

(c) HOS-NWT 2D Regular waves (d) HOS-NWT 2D Irregular waves

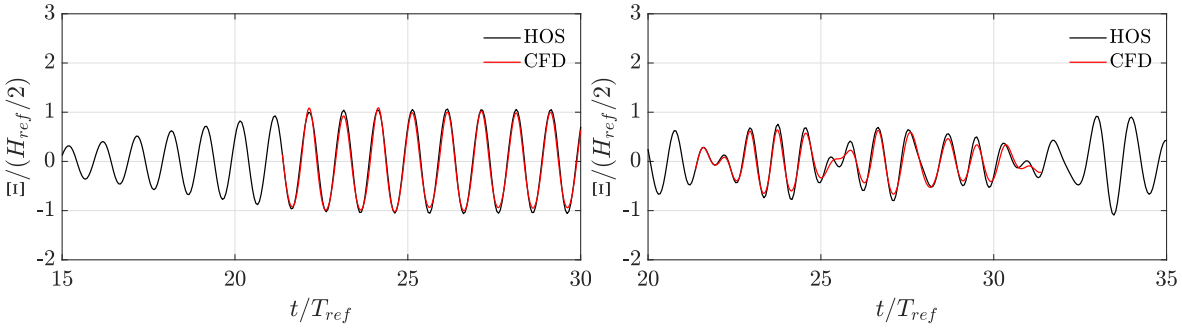

(e) HOS-NWT 3D Regular waves (f) HOS-NWT 3D Irregular waves

Fig. 10. Comparison between the reconstructed nonlinear HOS waves in CFD and HOS reference.

Table 3
Pearson correlation coefficient (r) between reference HOS wave elevation and the elevation of reconstructed HOS waves by the CFD solver.

Wave type	r
HOS-Ocean 2D Regular Waves	0.977
HOS-Ocean 2D Irregular Waves	0.980
HOS-NWT 2D Regular Waves	0.999
HOS-NWT 2D Irregular Waves	0.999
HOS-NWT 3D Regular Waves	0.996
HOS-NWT 3D Irregular Waves	0.977

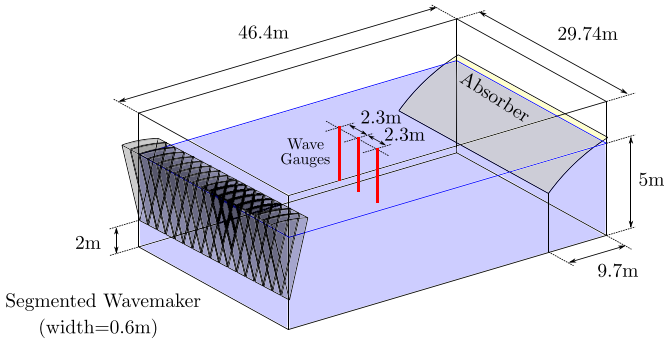

Fig. 11. Dimensions of the École Centrale de Nantes ocean wave tank.

The wave condition considered corresponds to the 1000-year return period sea state in the Gulf of Mexico (Bouscasse et al., 2021). The wave condition is given in Table 4. We consider only uni-directional waves.

In the severe sea state considered, breaking events will occur during wave propagation and need to be considered in the numerical model. Nonlinear potential flow solvers such as HOS are not adapted to the direct simulation of breaking waves, whose physical features need to be approximated by a dedicated model. The chosen approach within HOS considers the localized spatial and temporal damping due to wave breaking as described in Seiffert et al. (2017) and Seiffert and Ducrozet (2018). The localized damping is applied when the wave breaking is expected to occur during the HOS simulation. The identification uses a breaking onset criterion defined in Seiffert et al. (2017), Seiffert and Ducrozet (2018), and Barthelemy et al. (2018) as:

$$\frac{\mathcal{F}/\mathcal{E}}{v_p} = \frac{u_{crest}}{v_p} \geq B_{threshold} \tag{20}$$

where $\mathcal{F}$ is the local energy flux in the direction of wave propagation, $\mathcal{E}$ is the local energy density, v_p is the phase velocity of waves, u_{crest} is the horizontal velocity at the wave crest and $B_{threshold}$ is the threshold to determine the wave breaking, respectively. In the present study, $B_{threshold} = 0.85$ was selected from the experiments of Barthelemy et al. (2018), confirmed by the experiments of Seiffert et al. (2017).

Wave breaking events during the HOS simulation are identified and plotted in Fig. 12. The horizontal and vertical axes represent the spatial and temporal location of wave-breaking events during the simulation. A target wave breaking event is chosen at $x_{br}/\lambda_p = 5.6$ and $t_{br}/T_p = 100.0$. The adjacent time and space are needed for the CFD simulation; therefore, the spatial and temporal window of $t \in t_{br}+[-2T_p, 6T_p]$ and $x \in x_{br}+[-3.5\lambda_p, 4.5\lambda_p]$ is used. Lengths of inlet and outlet zones to generate/absorb waves are set to be $2\lambda_p$ and $3\lambda_p$, respectively. Three wave gauges are installed in experiments at the wave breaking position in the horizontal direction, which is perpendicular to the wave propagation direction, and the distance between wave gauges is 2.3 m as shown in Fig. 11.

A parametric study on the refinement of the computational grid of the CFD solver was conducted to obtain converged results. The spatial and temporal discretization are determined to have similar

Table 4
The extreme wave condition.

Item	Value
Wave spectrum	JONSWAP
Significant wave height (H_s)	17.5 m
Peak period (T_p)	15.5s
Peak magnification factor (γ)	2.6
Wavelength of peak period (λ_p)	375.1 m
Wave steepness (H_s/λ_p)	0.045
Scale ratio	1/100

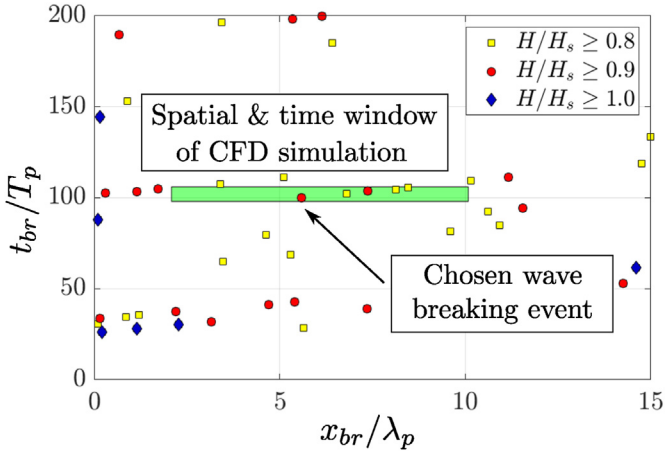

Fig. 12. Wave-breaking events identified during the HOS simulation and the chosen temporal and spatial window for the CFD simulation.

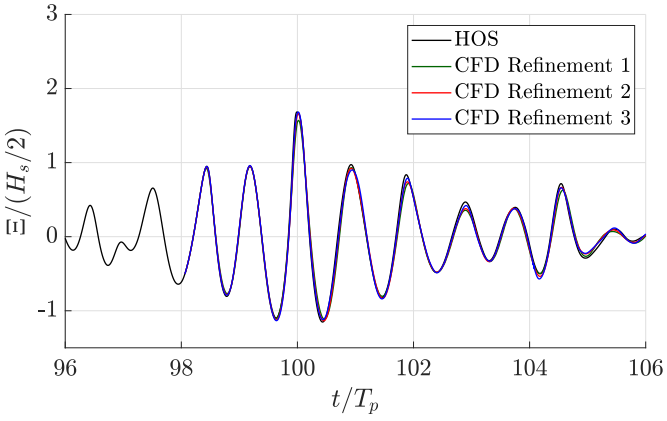

Fig. 13. Measured wave elevation at the wave breaking event with respect to the grid refinement of CFD simulation and HOS reference, x_br is the wave breaking position, and t_br is the time at the wave breaking event.

Table 5
Spatial and temporal refinement of numerical grids for CFD simulations.

Grid	$\lambda_p/\Delta x$	$H_s/\Delta z$	$T_p/\Delta t$
Refinement 1	62.5	18.4	300
Refinement 2	125	36.8	600
Refinement 3	250	73.5	1200

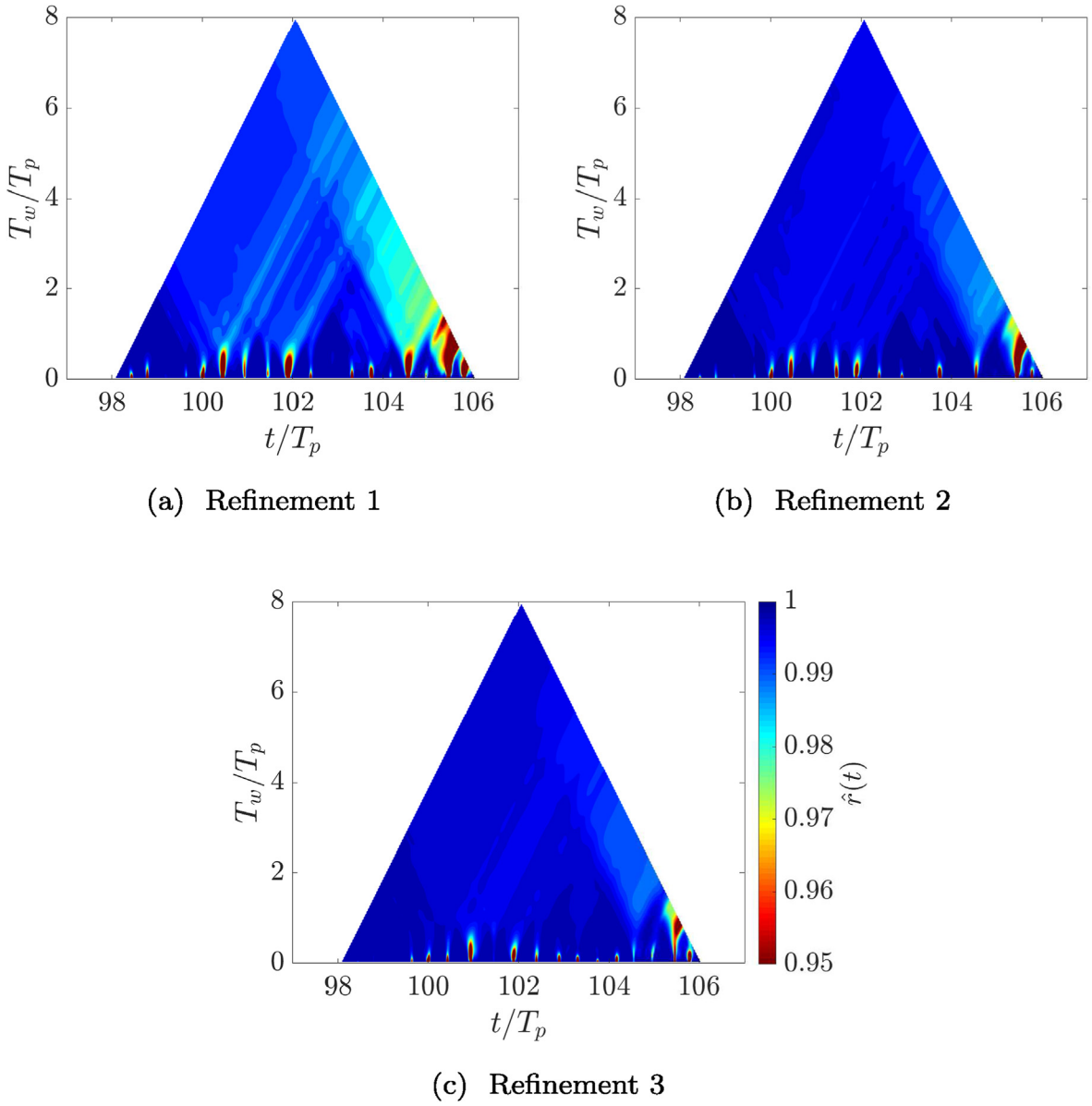

Fig. 14. Comparison of Pearson correlation coefficients of HOS reference and CFD measurements with different grid refinements.

values as in the previous studies (Bouscasse et al., 2021; Choi et al., 2020). The level of refinement is given in Table 5.

The wave elevations measured at the middle of the CFD computational domain are compared with the wave elevation obtained from the HOS simulation in Fig. 13.

The results of the CFD simulations with different refinements agree well with the HOS reference, even if the wave breaking model in HOS cannot reflect the exact mechanism of wave breaking. The Pearson correlation coefficients of two time-series data can be used to indicate the global agreement between two datasets, but a time-varying Pearson correlation coefficient can be useful to observe the evolution of discrepancy as discussed in Yule (1926). To observe a time-evolving local similarity score for two time-series data, Papadimitriou et al. (2006) introduced a Pearson correlation coefficient with a sliding window to localize the correlation estimations. A localized Pearson correlation coefficient between the HOS reference and each CFD measurement is compared in Fig. 14, where $\hat{r}(t)$ and T_w represent a localized Pearson correlation coefficient with a time-window of $t \in [t-T_w/2, t+T_w/2]$, and T_w represents the selected time window duration, respectively.

Values at the top corner of the triangles in Fig. 14 represent the Pearson correlation coefficient of the HOS reference and the CFD simulation for the whole CFD simulation time. The values are 0.992, 0.996, and 0.997 for the CFD Refinements 1, 2 and 3, respectively. Furthermore, the correlation between the HOS reference and the CFD simulations gradually decreases with the simulation time. However, the CFD case of a refined CFD computation grid keeps its correlation for the whole CFD simulation time.

Since the wave condition is extreme, many wave-breaking events were observed in experiments. Due to wave breaking and 3D effects of the wave tank, waves along the crest-line show only a slight disturbance. The snapshot at the breaking event, which corresponds to $t = 100s$, is shown in Fig. 15, together with the CFD simulation. A small spilling breaker is observed both in the experiment and CFD simulation.

The maximum, minimum, and average wave elevations from

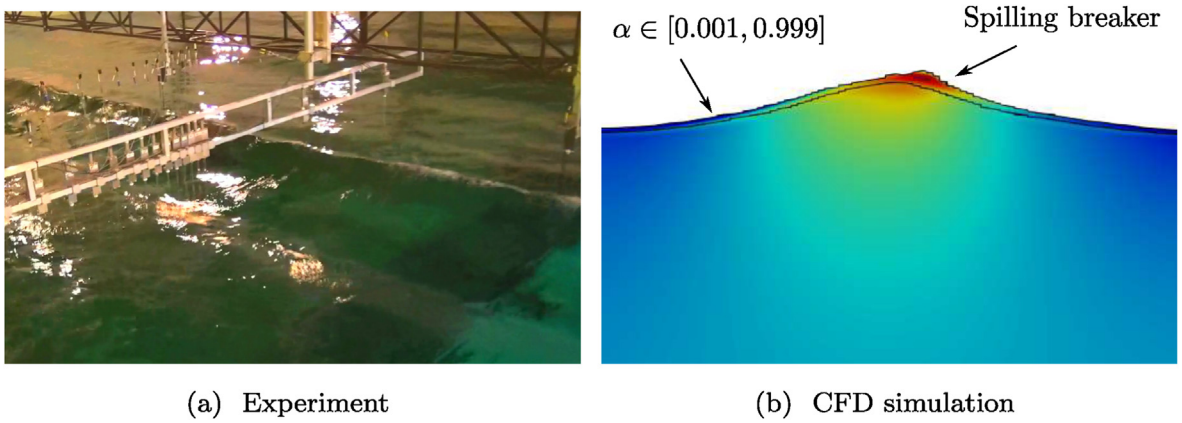

Fig. 15. Snapshot of wave breaking events in experiment and simulations.

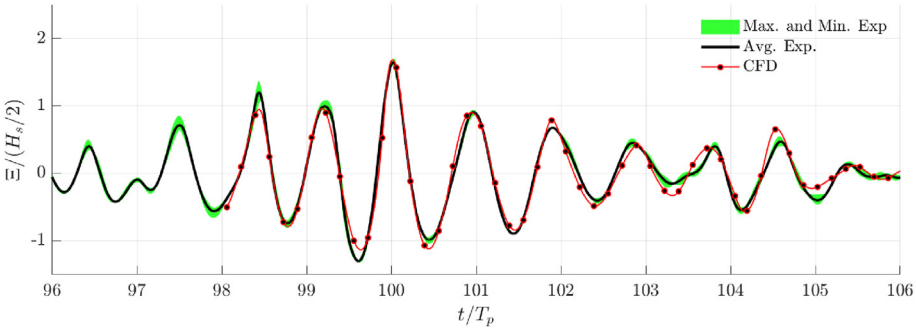

Fig. 16. Comparison between wave elevations of experiments and CFD simulations for extreme sea state at wave breaking point.

aligned wave gauges are taken because of the 3D effects that occur in the experiments. Wave elevations measured from the experiment are compared with the CFD simulation in Fig. 16. The wave elevation simulated and the experimental measurements agree overall. Furthermore, a small spilling wave breaking is observed in both experiment and CFD, which is promising regarding the capability of the coupled HOS-CFD simulation to model accurately extreme wave events. Some discrepancies are observed. The first reason might be related to experimental uncertainties induced by reflection from the physical beach being different from the one generated numerically as well as spurious currents, which makes the deterministic comparisons challenging to achieve perfectly. Another reason might be linked to the numerical model. Though the CFD is supposed to overcome the limitations of the HOS model and its simplified breaking model, the numerical domain is not as long as the physical one, and some effects can last.

6. Conclusions

This research describes and validates a reconstruction procedure of nonlinear irregular waves in CFD simulations. The nonlinear wave model is based on the HOS method, and the simple wave breaking model is used. Since the functional values are evaluated at the free-surface in the HOS method, the HOS waves are reconstructed in three-dimensional interpolation nodes. A couple of HOS wave fields near the time of interest are used for the interpolation for efficiency. The reconstruction algorithm based on the B-spline interpolation over space and time is proposed.

Because the vertical function used in the HOS method is a hyperbolic function and the energy in the low-frequency region moves to the high-frequency region due to nonlinear interaction, a large fluid velocity at the crest occurs when the extreme wave condition is considered. The reconstruction technique has been validated for long-crested and short-crested waves and for both HOS-Ocean and HOS-NWT solvers. The reconstructed wave elevation in CFD simulations shows good correlations with HOS results. Furthermore, the reconstructed wave elevation has been validated with experiments. The proposed reconstruction technique of nonlinear waves in the CFD solver has been validated on different types of sea states, including an extreme one with wave-breaking events.

Declaration of competing interest

The authors declare that they have no known competing financial interests or personal relationships that could have appeared to influence the work reported in this paper.

Acknowledgements

This study was supported by BK21 FOUR Graduate Program for Green-Smart Naval Architecture and Ocean Engineering of Pusan National University, the French National Research Agency (ANR) as part of the “Investissements d’Avenir” Programme (ANR-16-IDEX-0007), and Centrale Nantes - Bureau Veritas research chair.

References

Baronio, F., Wabnitz, S., Chen, S., Grelu, P., Conforti, M., 2015. Baseband modulation instability as the origin of rogue waves. In: 2015 Eur. Conf. Lasers Electro-Optics - Eur. Quantum Electron. Conf. Optical Society of America.

Barthelemy, X., Banner, M.L., Peirson, W.L., Fedele, F., Allis, M., Dias, F., 2018. On a unified breaking onset threshold for gravity waves in deep and intermediate

depth water. J. Fluid Mech. 841, 463–488. https://doi.org/10.1017/jfm.2018.93.
Bihs, H., Kamath, A., Alagan Chella, M., Arntsen, Ø.A., 2017. Extreme wave generation, breaking and impact simulations with REEF3D. In: Int. Conf. Offshore Mech. Arct. Eng..
Bonnefoy, F., Ducrozet, G., Le Touzé, D., Ferrant, P., 2009. Time-domain simulation of nonlinear water waves using spectral methods. In: Adv. Numer. Simul. Nonlinear Water Waves. World Scientific.
Bouscasse, B., Bockman, A., Ducrozet, G., Pakozdi, C., Kim, J.W., Croonenborghs, E., Lim, H., Bihs, H., Choi, Y.M., 2020. Development of a protocol to couple wave and CFD solvers towards reproducible cfd modeling practices for offshore applications. In: *Proceedings Of the International Conference On Offshore Mechanics And Arctic Engineering - OMAE*. Volume 1 of *International Conference On Offshore Mechanics And Arctic Engineering*. https://doi.org/10.1115/OMAE2020-19188, 10.1115/OMAE2020-19188.
Bouscasse, B., Califano, A., Choi, Y.M., Haihua, X., Kim, J.W., Kim, Y.J., Lee, S.H., Lim, H.-J., Park, D.M., Peric, M., Shen, Z., Yeon, S.M., 2021. Qualification criteria and the verification of numerical waves: Part 2: CFD-based numerical wave tank. In: Proc. ASME 2021 40th Int. Conf. Ocean. Offshore Arct. Eng.. OMAE2021–63710.
Canard, M., Ducrozet, G., Bouscasse, B., 2020. Generation of 3-hr long-crested waves of extreme sea states with HOS-nwt solver. Int. Conf. Offshore Mech. Arctic Eng. https://doi.org/10.1115/OMAE2020-18930, 10.1115/OMAE2020-18930.
Canard, M., Ducrozet, G., Bouscasse, B., 2022. Varying ocean wave statistics emerging from a single energy spectrum in an experimental wave tank. Ocean. Eng. 246, 110375. https://www.sciencedirect.com/science/article/pii/S0029801821016668, 10.1016/j.oceaneng.2021.110375.
Chen, H.C., 2013. CFD simulation of directional short-crested waveson jack-up structure. Int. J. Offshore Polar Eng. 23.
Choi, J., Yoon, S.B., 2009. Numerical simulations using momentum source wavemaker applied to RANS equation model. Coast. Eng. 56, 1043–1060. https://doi.org/10.1016/j.coastaleng.2009.06.009. https://www.sciencedirect.com/science/article/pii/S0378383909000970.
Choi, Y.-M., Gouin, M., Guillaume, D., Bouscasse, B., Ferrant, P., 2019. Grid2Grid. https://github.com/LHEEA/Grid2Grid.
Choi, Y.-M., Kim, Y.J., Bouscasse, B., Seng, S., Gentaz, L., Ferrant, P., 2020. Performance of different techniques of generation and absorption of free-surface waves in Computational Fluid Dynamics. Ocean. Eng. 214, 107575. https://doi.org/10.1016/j.oceaneng.2020.107575. https://www.sciencedirect.com/science/article/pii/S0029801820305837.
Damián, S.M., 2013. An Extended Mixture Model for the Simultaneous Treatment of Short and Long Scale Interfaces. Ph.D. thesis Universidad Nacional del Litoral.
De Boor, C., 1978. A Practical Guide to Splines. Springer-Verlag, New York.
de Hauteclocque, G., Rezende, F.C., Bigot, F., Derbanne, Q., 2017. A response conditioned wave approach for structural analysis of FPSOs presenting resonant second order roll motions. In: SNAME Offshore Symp.
Dommermuth, D.G., Yue, D.K.P., 1987. A high-order spectral method for the study of nonlinear gravity waves. J. Fluid Mech. 184, 267–288.
Ducrozet, G., Bonnefoy, F., Le Touzé, D., Ferrant, P., 2007. 3-D HOS simulations of extreme waves in open seas. Nat. Hazards Earth Syst. Sci. 7, 109–122. https://www.nat-hazards-earth-syst-sci.net/7/109/2007/, 10.5194/nhess-7-109-2007.
Ducrozet, G., Bingham, H.B., Engsig-Karup, A.P., Bonnefoy, F., Ferrant, P., 2012a. A comparative study of two fast nonlinear free-surface water wave models. Int. J. Numer. Methods Fluid. 69, 1818–1834. https://doi.org/10.1002/fld.2672. https://onlinelibrary.wiley.com/doi/abs/10.1002/fld.2672.
Ducrozet, G., Bonnefoy, F., Le Touzé, D., Ferrant, P., 2012b. A modified High-Order Spectral method for wavemaker modeling in a numerical wave tank. Eur. J. Mech. B Fluid 34, 19–34. https://doi.org/10.1016/j.euromechflu.2012.01.017. http://www.sciencedirect.com/science/article/pii/S0997754612000180.
Ducrozet, G., Bonnefoy, F., Le Touzé, D., Ferrant, P., 2016. HOS-ocean: open-source solver for nonlinear waves in open ocean based on High-Order Spectral method. Comput. Phys. Commun. 203, 245–254. https://doi.org/10.1016/j.cpc.2016.02.017. http://www.sciencedirect.com/science/article/pii/S0010465516300327.
Dysthe, K.B., Trulsen, K., Krogstad, H.E., Socquet-Juglard, H., 2003. Evolution of a narrow-ban spectrum of random surface gravity waves. J. Fluid Mech. 478, 1–10.
Elhanafi, A., Fleming, A., Macfarlane, G., Leong, Z., 2017. Numerical hydrodynamic analysis of an offshore stationary–floating oscillating water column–wave energy converter using CFD. Int. J. Nav. Archit. Ocean Eng. 9, 77–99. https://doi.org/10.1016/j.ijnaoe.2016.08.002.
Engsig-Karup, A.P., 2006. Unstructured Nodal DG-FEM Solution of High-Order Boussinesq-type Equations. Ph.D. thesis Technical University of Denmark Kgs. Lyngby.
Engsig-Karup, A.P., Eskilsson, C., 2019. Spectral element FNPF simulation of focused wave groups impacting a fixed FPSO-type body. Int. J. Offshore Polar Eng. 29, 141–148.
Fedele, F., Brennan, J., Ponce de León, S., Dudley, J., Dias, F., 2016. Real world ocean rogue waves explained without the modulational instability. Sci. Rep. 6.
Ferziger, J.H., Peric, M., 2012. Computational Methods for Fluid Dynamics. Springer Berlin Heidelberg. https://books.google.co.kr/books?id=ye3tCAAAQBAJ.
Forristall, G.Z., 2000. Wave crest distributions: observations and second-order theory. J. Phys. Oceanogr. 30, 1931–1943.
Frigo, M., Johnson, S., 2005. The design and implementation of FFTW3. Proc. IEEE 93, 216–231.
Fuhrman, D.R., 2004. Numerical Solutions of Boussinesq Equations for Fully Nonlinear and Extremely Dispersive Water Waves. Ph.D. thesis Technical University of Denmark Kgs. Lyngby.
Gatin, I., Vukčević, V., Jasak, H., 2017. A framework for efficient irregular wave simulations using Higher Order Spectral method coupled with viscous two phase model. J. Ocean Eng. Sci. 2, 253–267. https://doi.org/10.1016/j.joes.2017.09.003. http://www.sciencedirect.com/science/article/pii/S246801331730044X.
Goda, Y., 1999. A comparative review on the functional forms of directional wave spectrum. Coast Eng. J. 41, 1–20.
Hirt, C.W., Nichols, B.D., 1981. Volume of Fluid (VOF) method for the dynamics of free boundaries. J. Comput. Phys. 39, 201–225.
Hogg, R.V., McKean, J.W., Craig, A.T., 2005. Introduction to Mathematical Statistics. Pearson education international. Pearson Education. https://books.google.co.kr/books?id=dX4pAQAAMAAJ.
Jacobsen, N.G., 2017. Waves2Foam Manual. Technical Report Deltares, The Netherlands.
Jacobsen, N.G., Fuhrman, D.R., Fredsøe, J., 2012. A wave generation toolbox for the open-source CFD library: OpenFoam. Int. J. Numer. Methods Fluid. 70, 1073–1088. https://doi.org/10.1002/fld.2726. https://onlinelibrary.wiley.com/doi/abs/10.1002/fld.2726.
Jasak, H., 1996. Error Analysis and Estimation for the Finite Volume Method with Applications to Fluids Flows. Ph.D. thesis Imperial College.
Jasak, H., 2009. OpenFOAM: open source CFD in research and industry. Int. J. Nav. Archit. Ocean Eng. 1, 89–94. https://doi.org/10.2478/ijnaoe-2013-0011.
Kim, Y.J., 2021. Numerical improvement and validation of a naval hydrodynamics CFD solver in view of performing fast and accurate simulation of complex ship-wave interaction. Ph.D. thesis École Centrale de Nantes.
Kim, J.W., O'Sullivan, J., Read, A., 2012. Ringing analysis of a vertical cylinder by Euler overlay method. 31st Int. C. Ocean. Offshore Arct. Eng. OMAE2012–44915.
Larsen, B.E., Fuhrman, D.R., 2018. On the over-production of turbulence beneath surface waves in Reynolds-averaged Navier–Stokes models. J. Fluid Mech. 853, 419–460.
Lee, C.M., Park, S.C., Yu, J.W., Choi, J.E., Lee, I., 2019. Effects of diffraction in regular head waves on added resistance and wake using CFD. Int. J. Nav. Archit. Ocean Eng. 11, 736–749. https://doi.org/10.1016/j.ijnaoe.2019.02.013.
Li, Z., 2018. Two-phase spectral wave explicit Navier-Stokes equations method for wave-structure interactions. Ph.D. thesis École Centrale de Nantes.
Lu, X., Dao, M.H., Le, Q.T., 2022. A gpu-accelerated domain decomposition method for numerical analysis of nonlinear waves-current-structure interactions. Ocean. Eng. 259, 111901. https://doi.org/10.1016/j.oceaneng.2022.111901. https://www.sciencedirect.com/science/article/pii/S0029801822012410.
Mayer, S., Garapon, A., Sørensen, L.S., 1998. A fractional step method for unsteady free-surface flow with applications to non-linear wave dynamics. Int. J. Numer. Methods Fluid. 28, 295–315.
Miquel, A.M., Kamath, A., Alagan Chella, M., Archetti, R., Bihs, H., 2018. Analysis of different methods for wave generation and absorption in a CFD-based numerical wave tank. J. Mar. Sci. Eng. 6. https://www.mdpi.com/2077-1312/6/2/73, 10.3390/jmse6020073.
Papadimitriou, S., Sun, J., Yu, P.S., 2006. Local correlation tracking in time series. In: *Proc. - Sixth Int. Conf. Data Mining, ICDM 2006* Proceedings - IEEE International Conference on Data Mining, ICDM, pp. 456–465.
Perić, R., Vukčević, V., Abdel-Maksoud, M., Jasak, H., 2018. Tuning the Case-dependent Parameters of Relaxation Zones for Flow Simulations with Strongly Reflecting Bodies in Free-Surface Waves. ArXiv e-prints arXiv–1806.10995v2 [physics.flu–dyn]).
Rhee, S.H., Stern, F., 2002. RANS model for spilling breaking waves. J. Fluid Eng. 124, 424–432.
Rusche, H., 2002. Computational Fluid Dynamics of Dispersed Two-phase Flows at High Phase Fractions. Ph.D. thesis Imperial College.
Seiffert, B.R., Ducrozet, G., 2018. Simulation of breaking waves using the high-order spectral method with laboratory experiments: wave-breaking energy dissipation. Ocean Dynam. 68, 65–89.
Seiffert, B.R., Ducrozet, G., Bonnefoy, F., 2017. Simulation of breaking waves using the high-order spectral method with laboratory experiments: wave-breaking onset. Ocean Model. 119, 94–104.
Seng, S., Jensen, J.J., Malenica, Š., 2014. Global hydroelastic model for springing and whipping based on a free-surface CFD code (OpenFOAM). Int. J. Nav. Archit. Ocean Eng. 6, 1024–1040. https://doi.org/10.2478/IJNAOE-2013-0229. https://www.sciencedirect.com/science/article/pii/S2092678216302709.
Shen, Z., Wan, D., 2016. An irregular wave generating approach based on naoe-FOAM-SJTU solver. China Ocean Eng. 30, 177–192.
Sun, J., Ma, Z., Wang, D., Dong, S., Zhou, T., 2020. Numerical study of the run-up of a solitary wave after propagation over a saw-tooth-shaped submerged breakwater. Int. J. Nav. Archit. Ocean Eng. 12, 283–296. https://doi.org/10.1016/J.IJNAOE.2019.11.002.
Weller, H.G., Tabor, G., Jasak, H., Fureby, C., 1998. A tensorial approach to computational continuum mechanics using object-oriented techniques. Comput. Phys. 12, 620. https://doi.org/10.1063/1.168744.
West, B.J., Brueckner, K.A., Janda, R.S., Milder, M., Milton, R.L., 1987. A new numerical method for surface hydrodynamics. J. Geophys. Res. 92, 11803–11824.
Yule, G.U., 1926. Why do we sometimes get Nonsense Correlations between Time-Series? J. Roy. Stat. Soc. 89, 1–63.